# Interfacial dynamics of two immiscible fluids in spatially periodic porous media: The role of substrate wettability

Pranab Kumar Mondal, Debabrata DasGupta, and Suman Chakraborty*
*Department of Mechanical Engineering, Indian Institute of Technology Kharagpur, West Bengal 721302, India*
(Received 19 December 2013; revised manuscript received 24 April 2014; published 8 July 2014)

We delineate the contact line dynamics of two immiscible fluids in a medium having spatially periodic porous structures. The flow is driven by an external applied pressure gradient. We bring out the combined consequences of the solid fraction distribution and the substrate wettability on the resulting dynamics of the contact line, by employing phase-field formalism. We capture the sequence of spatiotemporal events leading to formation of liquid bridges by trapping a small amount of displaced phase fluid between two consecutive porous blocks, as dictated by the combinations of substrate wettability and solid fraction. We also demonstrate the existence of a regime of complete interfacial recovery, depending on the parametric space of the governing parameters under concern. Our results essentially demonstrate the intricate mechanisms by virtue of which the wettabilities of the substrates alter the dynamical evolutions of interfaces and the subsequent shapes and sizes of the adsorbed dispersed phases, bearing far-ranging consequences in several practical applications ranging from oil recovery to groundwater flow.

DOI: 10.1103/PhysRevE.90.013003 PACS number(s): 47.55.N−

## I. INTRODUCTION

A large number of physical processes involve the transport of fluids through porous pathways. Examples include oil recovery, hydrology, regeneration in chemical processes, fuel cells, groundwater flow, to name a few [1–3]. In order to unveil the underlying physics of flows pertinent to these applications, it is necessary to fully understand the governing physical processes at the pore scale. In many cases, the situation gets further complicated by the considerations of multiphase flows of immiscible fluids over interfacial scales, dictating the resultant larger-scale transport in a rather profound manner [3,4–8]. The underlying dynamics, in effect, is governed by the intricate interplay of different forces acting at the three-phase contact line and is a strong function of a number of factors, such as the length scales of the porous structure [9], the chemical characteristics of the surface [10], and the fluid rheology considered [11].

Interfacial dynamics at the pore scale and its influence in dictating the overall multiphase transport through porous media has been studied extensively, both numerically and experimentally [12–19]. Experimental studies have shown that the wetting properties of the fluids with regard to the solid substrate have a major effect on the formation and motion of the interface [20]. However, in order to capture the complete details of the interfacial behavior due to the wide range of the physical phenomena occurring in a pore-scale flow, experimental investigations may turn out to be challenging owing to two important factors: one is associated with the large-scale heterogeneity of the porous structures, while the other is essentially due to multidimensional and transient nature of the flow. The difficulties associated with detailed experimental investigations on the pore-scale flow of two immiscible fluids, in essence, have prompted the research community to adhere to empirical formalisms like Darcy's law [21] or its suitable variants [22]. While this approach may be somewhat effective for single-phase flows, difficulties do arise when situations concerning multiphase flows are encountered [23]. The complexities associated with the implementation of the interfacial boundary conditions for pore-scale polyphasic flows along with large-scale heterogeneity of the morphology of the porous structure necessitates the use of mathematical and numerical frameworks to model the intricate interplay of various forces and their combined influence in dictating the transport within the porous media [24–27].

It has been well established by the researchers that the presence of large-scale heterogeneity in conjunction with the wetting characteristics of the porous structure surface, which results because of the nature of the porous substrate and the contamination of various reagents, essentially plays a significant role in dictating the contact line motion, which significantly alters the imbibition dynamics [3]. However, a closer scrutiny of the available literature reveals that no prior studies exist that describe the contact line motion of two immiscible fluids in a periodic porous medium with specified substrate wettabilities. The scarcity albeit necessity for predicting the flow dynamics inside the porous media in presence of varying surface characteristics from fundamental consideration of contact line dynamics together with the assorted scale of the porous structure, accordingly, are the motivation of the present study.

In order to unveil the essential physics dictating the influence of the substrate wettability conditions on the dynamical evolution of two immiscible fluid phases, and at the same time in an effort to keep the key parametric variations and numerical computations tractable, we have considered idealized periodic porous media with simple circular obstacles having uniform surface wettabilities. Our results effectively demonstrate that the relative affinity of the substrates may alter the flow dynamics in a rather profound manner. Further, depending on the surface affinity condition and the solid fraction distribution, two distinctive dynamical regimes may be identified. We also show how the wettability condition alters the interface evolution dynamics and the subsequent shapes and sizes of the adsorbed dispersed phase.

*suman@mech.iitkgp.ernet.in

 

## II. THEORETICAL MODEL

### A. Problem description

We consider the flow of two immiscible fluids in a periodic porous medium. The representative volume element (RVE) of the porous medium mimics a two-dimensional pore structure with circular obstructions. Figure 1 shows the schematic of the periodic porous medium, the RVE and the computational domain considered in the present study. The computational domain is considered to be periodic along the $y$ direction, whereas along the $x$ direction we have considered a series of representative obstructions (four in the present study) in order to mimic the present flow scenario. It is important to note that the classical structure of the computational domain considered in the single-phase flow studies is the RVE itself with periodicity along both the $x$ and the $y$ directions. This treatment will, however, not work for the present case, as the application of the periodicity condition in the direction of the flow, for a multiphase flow scenario, will make the flow structure plug type and not mimic the physical reality.

We vary the size of the circular obstruction while keeping the size of the RVE fixed so as to vary the solid fraction. Four such solid fractions have been considered in the present study. Initially, the entire channel is filled with fluid B (shown by blue color or dark shade) and fluid A (shown by red color or light shade) enters the computational domain from the left end. In order to study the effect of the varying surface characteristics on the dynamics inside the porous media, we have considered the walls of the obstructions (circles in the present study) to be chemically patched with different predefined surface wettabilities, as manifested in terms of static contact angle $\theta_s$. The subscripts 1 and 2 are used to describe the properties of liquids A and B, respectively.

### B. Phase-field model for immiscible binary fluids

In the present study, we have used the phase-field model for describing the fluid motion in the capillary. In this context, we would like to mention here that a number of methods available in the literature have successfully been used in investigating the characteristics of multiphase flow hydrodynamics like volume of fluid (VOF) method [28], the level set method (LS) [29,30], and combined level set-VOF method (CLSVOF) [31]. However, the phase-field model has received a growing interest in the research community owing to several advantageous features inherent to this model [32–35]. A few such advantageous features include the existence of a thermodynamics basis, the implicit interface tracking capability, removal of stress singularity by introduction of slip at the fluid-solid interface, and fairly accurate mass conservation during the process. In the phase-field method, an order parameter $\phi$ is used to differentiate between two immiscible fluids in a binary fluids system. The order parameter describes the local fluid composition at any instant and is directly related to the scaled phase concentrations of the respective phases. In the present analysis, we define the order parameter as

$$\phi = (n_1 - n_2)/(n_1 + n_2), \tag{1}$$

where, $n_1$ and $n_2$ denote the number of molecules of the displacing phase fluid (fluid A in the present study) and the displaced phase fluid (fluid B in the present study), respectively. Therefore, the order parameter values of $\phi = 1$ and $-1$ indicate the bulk phases A and B, respectively. It is important to mention in this context here that, in the present study, the phase boundary separating the bulk phases is smooth and the Ginzburg-Landau free-energy functional for the two-phase system can be defined as the function of the order parameter as [33–40]

$$F = \int_{\forall} \left\{ f(\phi) + \frac{1}{2}\sigma\xi\,|\nabla\phi|^2 \right\} dV. \tag{2}$$

In Eq. (2), the first term is the bulk free-energy density, which is responsible for the immiscibility of the fluids, and the second term of Eq. (2) provides the excess free energy of the interface owing to the presence of the diffuse interface of finite thickness between the bulk phases. It is important to mention that $\sigma$ and $\xi$ appearing in Eq. (2) denote the surface energy per unit area and the order of the diffuse interface thickness, respectively. The form of the double-well potential $f(\phi)$ may be expressed in the form [34]

$$f(\phi) = \frac{\sigma}{4\xi}(1 - \phi^2)^2, \tag{3}$$

where the two minima ($\phi = \pm 1$) correspond to the two stable phases A and B, respectively.

The chemical potential $\mu$ is defined as the variational derivative of free energy, with respect to the order parameter $\phi$, and is given by

$$\mu = \frac{\delta F}{\delta \phi} = f'(\phi) - \sigma\xi\nabla^2\phi. \tag{4}$$

The interface profile in equilibrium condition may be obtained by setting $\mu(\phi) =$ constant.

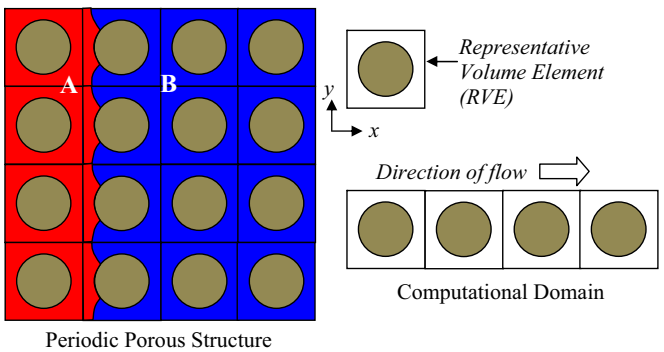


FIG. 1. (Color online) Schematic of the porous structure, the representative volume element (RVE), and the computational domain.

### C. Cahn-Hilliard model coupled with Navier-Stokes system of equations

In order to obtain the time-dependent interface profile, it is customary to describe the evolution of the order parameter $\phi$ in the flow field. The Cahn-Hilliard equation describes the order parameter evolution accounting the advective transport due to the presence of the velocity field. The complete form of the convective Cahn-Hilliard equation can be expressed as

follows [41,42]:

$$\frac{\partial \phi}{\partial t} + \mathbf{u} \cdot \nabla \phi = \nabla \cdot (M \nabla \mu). \tag{5}$$

Here, $M > 0$ is a mobility constant, which controls the diffusion across the interface. For the governing transport equation of the order parameter evolution [Eq. (5)], we define the following boundary conditions [43]:

$$\nabla \mu \cdot \mathbf{n} = 0, \tag{6a}$$

$$\mathbf{n} \cdot \nabla \phi = -\tan\left(\frac{\pi}{2} - \theta_s\right) |\nabla \phi - (\mathbf{n} \cdot \nabla \phi)\, \mathbf{n}|, \tag{6b}$$

where, $\mathbf{n}$ is the normal vector pointing outward from the solid surface.

It is important to mention in this context that the boundary condition given in Eq. (6a) indicates zero flux through the surface, whereas Eq. (6b) is the natural boundary condition, which essentially ensures specified contact angle $\theta_s$ at the boundary such that the order parameter remains approximately constant along the tangent to the interface [43].

The evolution equation for the order parameter is coupled with the Navier-Stokes equation. The Navier-Stokes equation is augmented with body force term $\mu \nabla \phi$, which is representative of the surface tension forcing. For a detailed derivation of the related force arising because of the presence of the interface, one may refer to an earlier review by Jacqmin [44]. The Navier-Stokes equation, including the body-force terms can be written in the form

$$\rho\left(\frac{\partial \mathbf{u}}{\partial t} + \mathbf{u} \cdot \nabla \mathbf{u}\right) = -\nabla p + \nabla \cdot [\eta\{(\nabla \mathbf{u}) + (\nabla \mathbf{u})^T\}] + \mu \nabla \phi, \tag{7a}$$

$$\nabla \cdot \mathbf{u} = 0, \tag{7b}$$

where, $p$ is the pressure. The fluid properties like the density and viscosity are considered to be functions of the order parameter and are given by [33,35]

$$\rho = \rho_A \left(\frac{1+\phi}{2}\right) + \rho_B \left(\frac{1-\phi}{2}\right), \tag{8a}$$

$$\eta = \eta_A \left(\frac{1+\phi}{2}\right) + \eta_B \left(\frac{1-\phi}{2}\right). \tag{8b}$$

The boundary conditions considered for all the simulations are given below:

$$\text{At the inlet}: \quad u = u_m, \tag{8c}$$

$$\text{At the outlet}: \quad p = p_0, \tag{8d}$$

$$\text{At the solid surface}: \quad u = 0. \tag{8e}$$

The complete set of governing transport equations describing the motion through the narrow fluidic pathways of the porous microstructure is given by the Eqs. (5) and (7), coupled with the boundary condition for $\phi$ as given by Eq. (6). For the Navier-Stokes equations, we use the standard no-slip boundary condition for at the walls, as well as velocity inlet and pressure outlet boundary conditions on the inlet and outlet boundaries mentioned in Eqs. (8c)–(8e).

*Nondimensionalization of the governing transport equations.* Here, we adopt the following nondimensionalization scheme: $\bar{u} = u/u_{\text{ref}}$; $\bar{v} = v/u_{\text{ref}}$; $\bar{x}, \bar{y} = x/\xi, y/\xi$; $\bar{\eta} = \eta/\eta_{\text{ref}}$; $\bar{\rho} = \rho/\rho_{\text{ref}}$; $\bar{p} = p/p_{\text{ref}}$, and $\bar{t} = t/t_{\text{ref}}$ where $p_{\text{ref}} = \eta_{\text{ref}} u_{\text{ref}}/\xi$; $t_{\text{ref}} = \xi/u_{\text{ref}}$. The scale for nondimensionalization of the chemical potential is given as $\bar{\mu} = \mu/(\sigma/\xi)$. Upon implementation of the above scheme of nondimensionalization, we finally arrive at the following set of dimensionless equations:

$$\frac{\partial \phi}{\partial \bar{t}} + \mathbf{u} \cdot \nabla \phi = \frac{1}{\text{Pe}} \nabla . (\bar{M} \nabla \bar{\mu}), \tag{9}$$

$$\text{Re} \cdot \bar{\rho}\left(\frac{\partial \bar{\mathbf{u}}}{\partial \bar{t}} + \bar{\mathbf{u}} \cdot \nabla \bar{\mathbf{u}}\right) = -\nabla \bar{p} + \nabla \cdot [\bar{\eta}\{(\nabla \bar{\mathbf{u}}) + (\nabla \bar{\mathbf{u}})^T\}] + \frac{1}{\text{Ca}} \bar{\mu} \nabla \phi, \tag{10}$$

$$\nabla \cdot \bar{\mathbf{u}} = \mathbf{0}. \tag{11}$$

The scheme of nondimensionalization leads to a few dimensionless parameters given as

$$\text{Peclet number (Pe)} = u_{\text{ref}} \xi^2 / M_c \sigma.$$
$$\text{Capillary number (Ca)} = u_{\text{ref}} \eta_{\text{ref}} / \sigma.$$
$$\text{Reynolds number (Re)} = \rho_{\text{ref}} u_{\text{ref}} \xi / \eta_{\text{ref}}.$$

In Eq. (9), $\bar{M}$ is defined as: $\bar{M} = M/M_c$. The value of the mobility parameter, $\bar{M}$ has an important bearing on the stability of the solution and the increasing value of mobility parameter stabilizes the flow [45]. In our present numerical experimentation, we define $M_c$ following reported molecular dynamics simulation studies [46] as $M_c = C \frac{l^4}{\sqrt{\tilde{m}\varepsilon_e}}$, where $l$ and $\varepsilon_e$ are the length scale and energy scale in the Lennard-Jonnes potential for fluid molecules, respectively, and $\tilde{m}$ is the molecular mass of fluid, and $C$ is a constant (given by 0.023), so as to ensure the convergence of the solution. It is important to note that in the nondimensionalization scheme, one can use either of the fluid properties to be the reference values of the different fluid properties (like viscosity and density) to define the two-phase flow configuration. In the present study, we have considered the properties of fluid A as the reference properties. We do mention here that apart from the dimensionless parameters mentioned above, the ratios of different fluid properties, such the density ratio, $\rho_r = \frac{\rho_B}{\rho_A}$, and the viscosity ratio, $\eta_r = \frac{\eta_B}{\eta_A}$, play an important role to on the interfacial dynamics. Please note that in the present study, we consider density and viscosity matched immiscible binary fluids for all our simulations.

Keeping in view the wide variety of substrate wettability conditions encountered in reality, in the present study, we have considered a range of values of the static contact angle $\theta_s$ in order to gain insight into all the anticipated flow scenarios.

We consider the flow to be driven by an external velocity field where an average velocity $u_{\text{avg}} = 0.2$ is taken in the analysis that corresponds to value given in Ref. [35]. It is important to be noted here that the scheme of nondimensionalization does not alter the form of the boundary conditions used in the present study; rather it replaces all the variables by the corresponding nondimensional ones. In the subsequent sections, we will drop the overbars from the variables for clarity of representation. In Fig. 2, we show the governing transport equations along with the appropriate boundary conditions schematically. In the present study, we have used unstructured triangular meshes

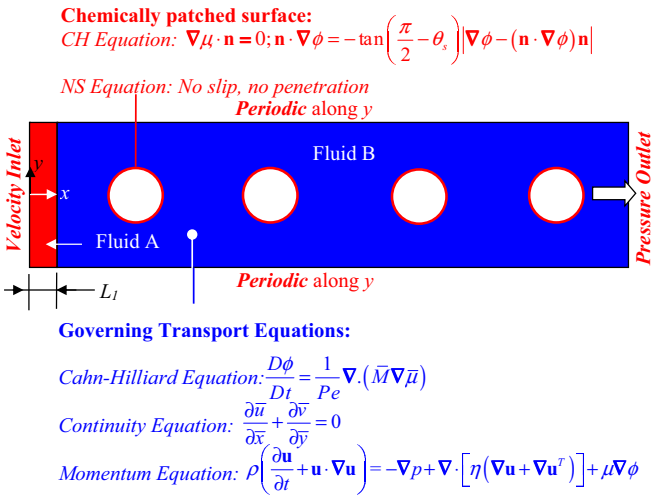


FIG. 2. (Color online) Schematic of the problem domain delineating the governing transport equations and boundary conditions. The channel is initially filled with fluid B (shown in blue color or dark shade) and fluid A (shown by red color or light shade) enters the channel from the left.

generated using advancing front technique where maximum element size is restricted to less than $0.5\xi$. Even though the mesh is nonorthogonal it is conformal. A mesh resolution of $0.5\xi$ is sufficient to resolve the interface as indicated in a number of previous studies [33,35]. For all numerical experimentations carried out in the present study, we have used the commercial software package COMSOL. The numerical framework used in the present study is benchmarked with the results reported by Wang *et al.* [35].

## III. RESULTS AND DISCUSSIONS

The main aim of the present study is to instigate the evolution of the interface of two immiscible fluids over porous structures having different surface wettabilities. Toward this, we note that the interfacial dynamics is strongly dictated by the following parameters: (i) solid fraction of the porous media ($f_s$), (ii) the wettability of the porous structures as manifested in terms of static contact angle specified at the surface ($\theta_s$). The solid fraction $f_s$ is defined as the ratio of volume (or area for the 2D case presented here) of solid obstacles to the volume of the RVE. In the present study we have considered four different solid fractions $f_s \in [0.15,0.26,0.4,0.51]$ and seven different substrate wettabilities as governed by $\theta_s \in [45^\circ,60^\circ,75^\circ,90^\circ,105^\circ,120^\circ,135^\circ]$. The values of the other dimensionless parameters have been chosen as $\mathrm{Pe}=0.2, \mathrm{Re}=0.03$, and $\mathrm{Ca}=0.083$ and are assumed to be constant throughout the analysis unless otherwise mentioned.

In order to instigate the effect of substrate wettability on the evolution of the interface and the resultant capillary filling dynamics, we show the time sequence of the interface evolution for $\theta_s=60^\circ$ and $\theta_s=120^\circ$ representative of different wettability scenarios for $f_s=0.25$.

It is important to note that the two image sequences shown in Fig. 3 depict two distinctive regimes of interface evolution. In the left series (which corresponds to $\theta_s=60^\circ$), we observe a

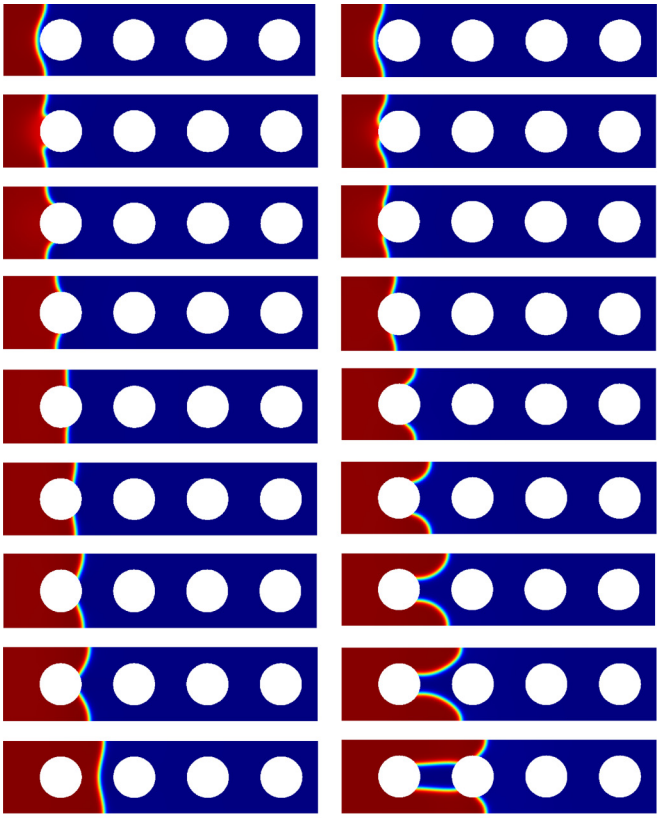


FIG. 3. (Color online) Time sequence of interface evolution $f_s=0.25$ and (a) $\theta_s=60^\circ$ at nondimensional times of $\bar{t}=40$, 45, 50, 60, 70, 80, 90, 100, and 140 and (b) $\theta_s=120^\circ$ at nondimensional times of $\bar{t}=40$, 45, 50, 60, 80, 100, 130, 150, and 180.

complete recovery of the interface as the interface moves from one RVE to the other. In the right series (which corresponds to $\theta_s=120^\circ$), on the other hand, we observe the formation of liquid bridge between the successive obstacles.

Quite notably, the shape and size of the liquid bridge formed between two consecutive porous blocks keeps on changing until it acquires a steady-state configuration. Once the liquid bridge attains a steady configuration, its shape and size does not change appreciably any further. We confirm this phenomena from Fig. 4, where we show the interface evolution at nondimensional times of 160 and 260, respectively. One can see that the shape and size of the liquid volume trapped between first two porous blocks remains unchanged with time and does not get altered by the surrounding flows.

In Fig. 5, we show the velocity vector plots depicting the flow structure for the two cases shown above viz. complete interface recovery and bridge formation. It is interesting to note that the evolving interface significantly alters the flow

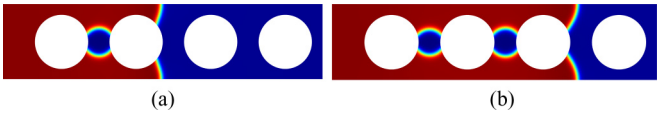


FIG. 4. (Color online) Interface evolution for $f_s=0.4$ and $\theta_s=60^\circ$ at nondimensional times of 160 and 260, respectively.

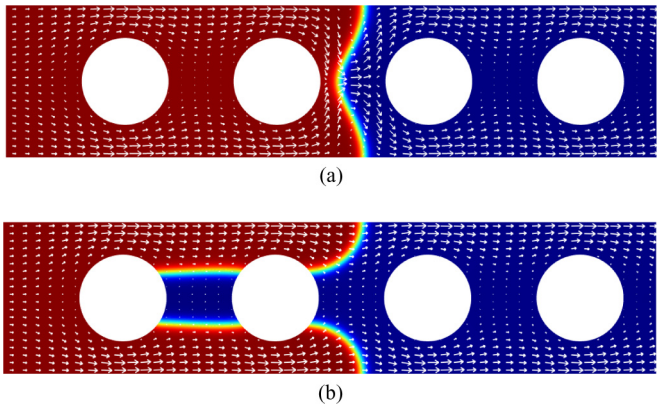

FIG. 5. (Color online) Velocity vector plot depicting the flow structure for $f_s = 0.25$ and (a) $\theta_s = 60^\circ$ and (b) $\theta_s = 120^\circ$ at nondimensional times of 160 and 220, respectively.

structure. Also, there is no significant flow through the surface of the liquid bridge primarily due to the location of the bridge, which forms between the successive blocks.

In order to understand the underlying mechanism responsible for this distinctive behavior, we try to explore the influence of the substrate wettability on the contact line dynamics and its eventual role in dictating the transport. As the interface progresses and first encounters the solid obstacle, it essentially subtends zero angle with the surface. As soon as the interface touches the surface, contact line forms, which, due to symmetry of the obstacle, progresses symmetrically along the top and the bottom edges of the circular obstacle as clearly evident from Fig. 3. At the instant when the contact line forms, the contact angle is close to zero (since the interface touches the obstacle tangentially) and the interface at the contact line subsequently relaxes in an effort to attain the dynamic contact angle depending on the surface wettability. Therefore, initially the contact line velocity is very high and it decreases as the interface relaxes with time. The similar trend is observed in Fig. 6, where we show the variation of the velocity of the moving contact line (tangential to the obstacle surface) with

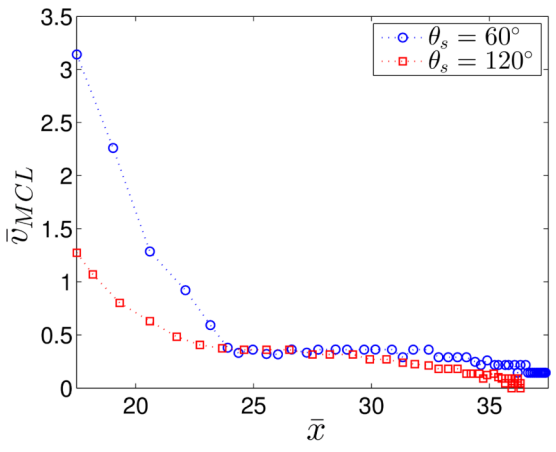


FIG. 6. (Color online) Variation of the velocity of the moving contact line (tangential velocity along the obstacle surface) with axial location of the contact line for two different values of surface wettability $\theta_s = 60^\circ$ and $120^\circ$, respectively.

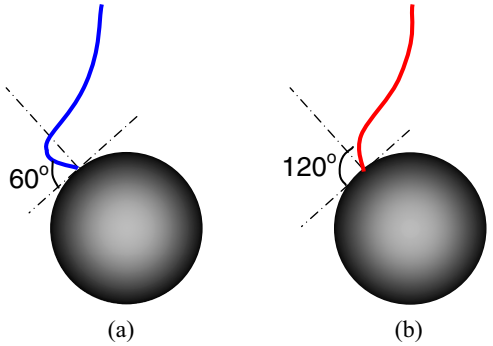


FIG. 7. (Color online) Schematic representation of the interface showing the contact line for (a) $\theta_s = 60^\circ$ and (b) $\theta_s = 120^\circ$.

axial distance for the two cases discussed above i.e., $f_s = 0.25$ and $\theta_s = 60^\circ/120^\circ$.

In Fig. 7, we depict a representation of the interface showing the contact line. The variations in contact angle made by the interface with the solid substrate are different because of the variations in the surface wettability conditions. It is important to note that because of the variation in surface affinity conditions, the conditions at the contact line at the instant of its formation are more severe with respect to its dynamic equilibrium condition. The term "dynamic equilibrium" is loosely employed in the present context to merely emphasize that the interface evolves dynamically and it will not reach its equilibrium configuration. The local contact angle eventually reaches the dynamic contact angle value, which will in turn keep on changing because of the substrate curvature. However, its variation is much less compared to the variation of the contact angle during the initial phase of the transience for the case with $\theta_s = 60^\circ$, as compared to that for $\theta_s = 120^\circ$. As a result of this, the magnitude of contact line velocity during the initial phase is more for case with $\theta_s = 60^\circ$ compared to $\theta_s = 120^\circ$, which is also evident from Fig. 6. As the contact line moves and it relaxes, its velocity decreases monotonically at a faster rate till a point when the interface has adjusted considerably and it roughly occurs when the point of inflection, existing on the interface joining the periodically repeating obstacles, vanishes (see third instance of Fig. 3(a) and fourth instance of Fig. 3(b). Beyond this point, the decrease in contact line velocity is somewhat slower. Since fluid A is displacing fluid B in the porous pathways, the mobility of the contact line will be more when the surface has affinity toward fluid A. The same trend is observed in Fig. 6, where we see that the contact line velocity is more when $\theta_s = 60^\circ$, as compared to $\theta_s = 120^\circ$. For $\theta_s = 120^\circ$, the contact line velocity drops to zero and contact line pinning is observed. This appears to be clearer from Fig. 8. From Fig. 8, we show the variation of the axial location of the contact line with time and we see the interface stalling toward the end of the obstacle. In the inset, we have shown the location of the point of stalling for three different surface affinity conditions. It is important to note that as $\theta_s$ increases and the affinity of the surface toward fluid B increases, the point of interface pinning shifts toward the upstream direction, i.e., toward the left. This shifting of the point of pinning with variation in surface affinity condition has

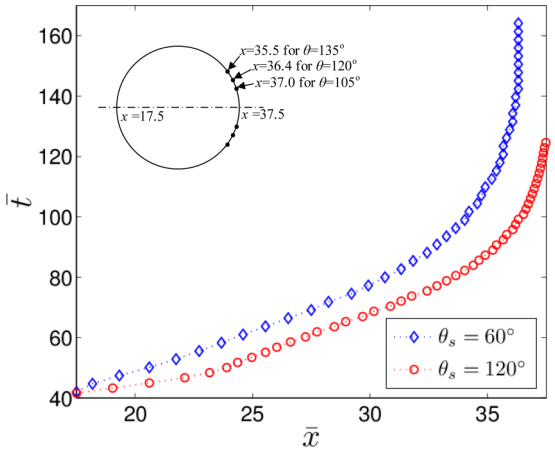


FIG. 8. (Color online) Variation of the $x$ component of the contact line location with time for $f_s = 0.25$ for two different values of surface wettability $\theta_s = 60°$ and 120°, respectively. In the inset, we show the location of stalled interface with variation in the static contact angle.

important consequences as will be discussed in a subsequent section.

Till this point, we have tried to focus our attention on the dynamics of the contact line. Next, let us try to look at the interface as a whole, evolving between two successive periodic obstacles as shown in Fig. 9, where we have shown the periodic repeats of half of the domain.

As the interface evolves with time, two distinctive features are observed. When the substrate preferentially likes fluid A, the mobility of the contact line is more and we see complete recovery of the interface; i.e., the two contact lines moving along the upper and the lower halves of the obstacles merge together to form a single interface again. On the other hand, when the substrate wettability is such that it preferentially likes fluid B, the contact line velocity is relatively lower and we observe contact line pinning. As a result of which, with passage of time, the evolving interface touches the obstacle located on the downstream RVE and we observe formation of a new contact line. This leaves behind a liquid bridge of fluid B between the two consecutive obstacles. However, this is not a universal phenomenon. It not only depends on the surface affinity condition but also on the solid fraction, as

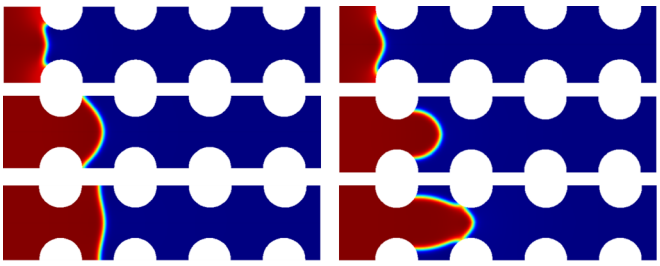


FIG. 9. (Color online) Evolution of the interface and existence of distinctive regimes for $f_s = 0.4$ and (a) $\theta_s = 60°$ corresponding to complete interface recovery and (b) $\theta_s = 120°$ corresponding to formation of liquid bridge

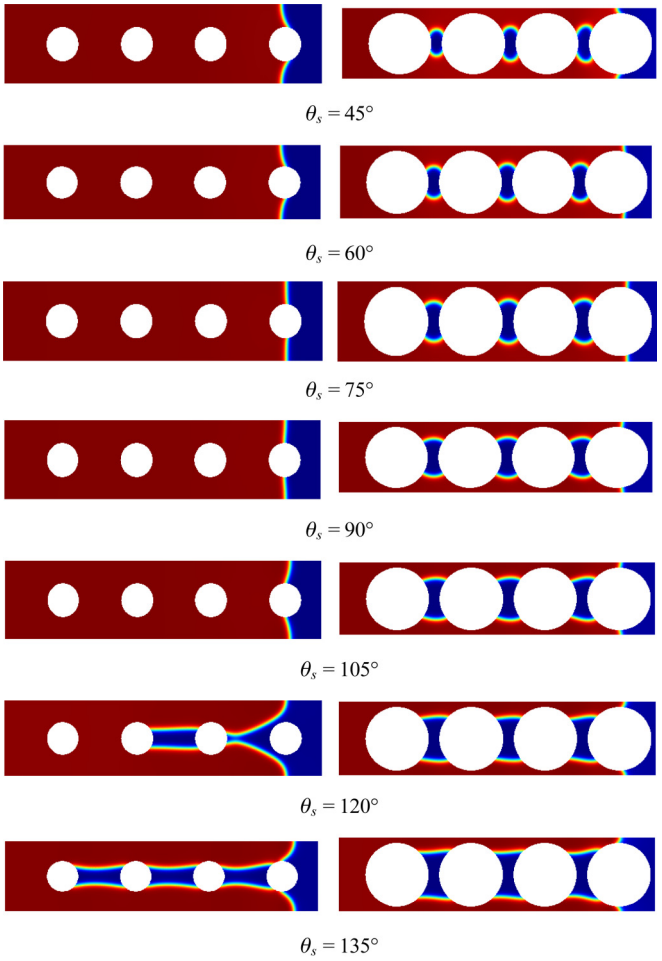


FIG. 10. (Color online) Interface evolution for solid fraction (a) $f_S = 0.15$ and (b) $f_S = 0.51$, obtained at different wetting conditions of the porous structure surface ($\theta_s = 45°, 60°, 75°, 90°, 105°, 120°, 135°$). The liquid bridge between two consecutive porous blocks for $f_s = 0.15$ is formed for $\theta_s = 120°$ and 135°, whereas for $f_s = 0.51$ liquid bridge forms for all the wetting conditions.

the variation of the solid fraction alters the distance between the obstacles and significantly alters the filling dynamics. In the subsequent discussions, we will systematically observe the influence of interesting interplay of the substrate wettability and solid fraction on the interfacial dynamics.

In an effort to construct a regime diagram clearly indicating the different regimes of dynamics, we try to explore the effect of variation of governing parameters viz. surface affinity conditions and solid fraction on the flow dynamics. In Fig. 10, we show the variation in the interface profiles with change in surface affinity condition of the obstacle for the two extreme solid fractions considered in the present study, i.e., 0.15 and 0.51.

For the value of solid fraction $f_s = 0.15$, which is the highest permeable porous structure considered in the present study, the complete recovery of the advancing fluid front is possible for $\theta_s \in [45°, 105°]$, whereas for $\theta_s = 120°$ and 135°, we observe the formation of a liquid bridge between two

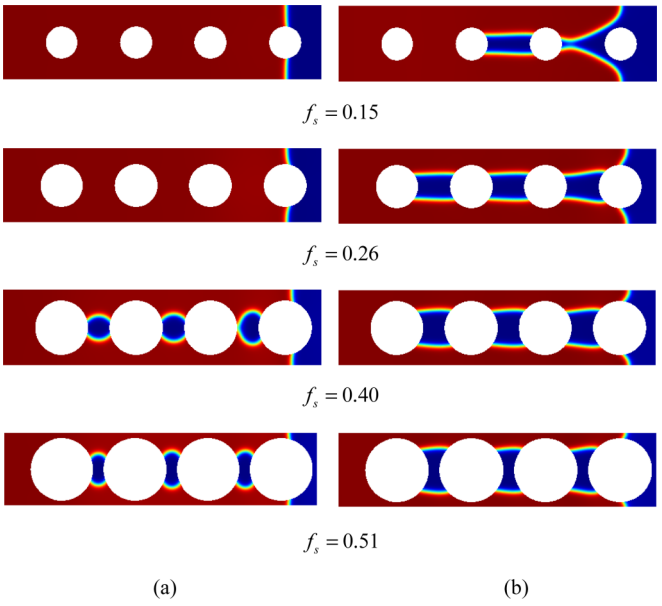


FIG. 11. (Color online) Interface evolution for surface wettability (a) $\theta_s = 60^\circ$ and (b) $\theta_s = 120^\circ$ for four different solid fractions considered in the present study ($f_S = 0.15, 0.26, 0.40, 0.51$). For $\theta_s = 60^\circ$, complete interface recovery is observed for $f_s = 0.15$ and 0.26, whereas liquid bridge formation is observed for $f_s = 0.40$ and 0.51. On the other hand, for $\theta_s = 120^\circ$, formation of liquid bridge is observed for all the solid fractions considered in the present study. The shape and size of the bridge, however, varies with the solid fraction.

consecutive porous blocks. It is important to note that for $\theta_s = 105^\circ$, we do not observe the formation of any liquid bridge for $f_s = 0.15$, while for all the other solid fractions we observe bridge formation. This can easily be explained from the fact that with increase in the value of $\theta_s$, the point of pinning shifts toward the left. For $f_s = 0.15$, because of smaller dimension of the obstacle, the distance between the points of pinning, which are toward the extreme right, is of the order of the interface width and we observe that the two contact lines interact with each other and merge, recovering the advancing front. For even lower dimension of the obstacles, the start of formation of liquid bridge will be shifted toward even higher value of $\theta_s$, and on the contrary, for very large obstacle dimension, there are chances of bridge formation from very low value of $\theta_s$. This will be more clear from the interface evolution for $f_s = 0.51$, which is the lowest permeable structure considered in the present study. For $f_s = 0.51$, we observe the formation of liquid bridge for all the values of $\theta_s$ considered in the present study. However, with increase in the value of $\theta_s$, as the pinning point shifts toward the left, the volume of displaced liquid trapped between the blocks increases and so is the shape of the liquid bridge.

In order to delve deep into the combined influence of the surface wettability and the solid fraction on the interface evolution behavior, next we try to explore the influence of variation of solid fraction on the filling dynamics. In Fig. 11, we show the variation in the interface profiles with change is solid fraction for two surface wettability conditions given by $\theta_s = 60^\circ$ and $120^\circ$. We see that for relatively low-porosity porous medium, i.e., when $f_s$ is high, liquid bridge forms even

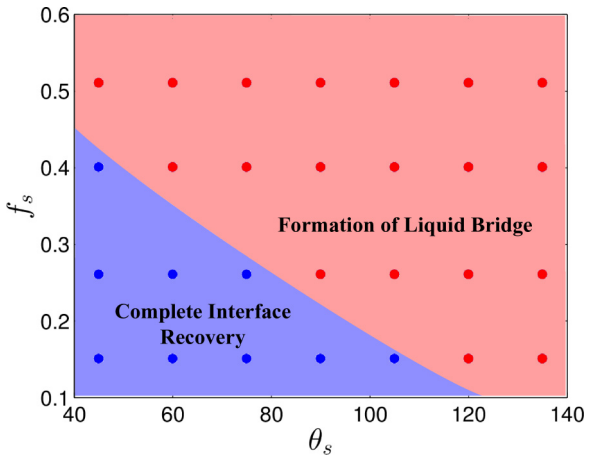


FIG. 12. (Color online) Regime diagram clearly depicting the regimes of interface evolution dynamics and its variation with solid fraction and wettability.

when the $\theta_s$ is low, whereas for high-porosity porous media we obtain complete interface recovery when $\theta_s$ is low and formation of liquid bridge when $\theta_s$ is high.

From the preceding discussions, it is clear that the intricate interplay between the surface wettability and the solid fraction of the porous medium plays interesting role in dictating the transport and in the resulting dynamics. In particular, we observe two distinctive regimes, viz. complete interface recovery and formation of liquid bridge. In Fig. 12, in a regime diagram, we show the two regimes of operation and the role of the governing parameters on the same.

We observe complete interface recovery when both $f_s$ or $\theta_s$ are small, i.e., when the obstacle dimensions are small and the surface has preferential affinity toward the displacing fluid. With increase in $f_s$ or $\theta_s$ or both, the chances of formation of liquid bridge increase.

Before we conclude, we would like to point out that the bridge formation highlighted in the preceding sections is not

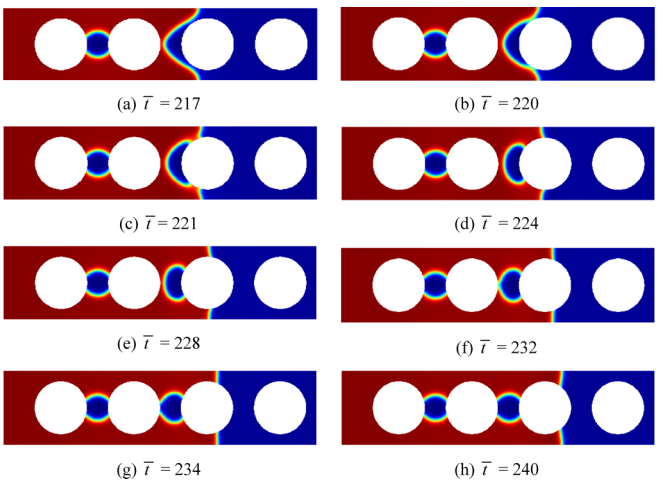


FIG. 13. (Color online) Time sequence plot of the interface of two immiscible fluids moving through porous medium, for $f_s = 0.40$ and $\theta_s = 60^\circ$. The snapshots obtained at different times show the interface breaking phenomenon and the dynamic evolution of the pinched-off portion.

the only mechanism of fluid trapping. We have also observed a second mechanism of trapping. This happens even after the interface has completely recovered after confronting one obstacle, when the curvature of the recovered interface at the line of symmetry is very small. In this case, it is possible that the two ends of the moving interface will touch the downstream obstacle after it travels for a while and we observe formation of two contact lines and a trapped liquid phase upstream of the obstacle. This will be more clear from the interface evolution structure shown in Fig. 13, where we show the time evolution of the interface for the case when the solid fraction $f_s = 0.40$ and $\theta_s = 60^\circ$. The snapshots taken at different instants of time clearly portray how the interface breaks as it moves over the porous structures. Depending upon the affinity condition of the obstacle and the amount of the displaced phase fluid trapped behind the obstacle, its shape will evolve with time owing to dynamic adjustment of contact angle with the solid surface.

## IV. CONCLUSIONS

In the present study, we address the interfacial dynamics of two immiscible fluids in a porous medium, which strongly depends on two important factors: the solid fraction of the medium and the surface wettability of the porous structure. We employ phase-field formalism to capture the underlying effects. We show how the substrate wettability–solid fraction combination alters the interfacial dynamics significantly and leads to several interesting events as the interface moves from one RVE to the other. Before concluding, we would like to highlight several interesting insights, which have been carefully observed from our study as given below:

(1) The velocity of the contact line, formed over the solid substrate, keeps on changing as the interface progresses over the porous blocks. Such alterations of contact line velocity, tuned by the interplay of the substrate wettability and pore fraction eventually leads to the stalling of the interface following the pinning of contact line. The phenomenon of interface stalling has important consequences as reflected either through the formation of liquid bridge by trapping a small amount of displaced phase fluid between two consecutive porous blocks or a complete recovery of the displaced phase fluid.

(2) We show existence of bridge formation when the surface wetting conditions preferentially like the displaced phase fluid and the tendency of bridge formation increases with the increase in substrate wetting strength. We also show that with increase in permeability of the porous media, the location of the interface stalling shifts toward the downstream direction eventually leading to a decreasing tendency of bridge formation with increase in porosity.

(3) We argue that the interesting interplay of the porosity of the media and the substrate wettability do have an interesting role to play on the pore-scale transport and, essentially, on the resulting core-scale imbibition dynamics. We identify the suitable combination of above two important parameters, i.e., $f_s$ and $\theta_s$, for which either a complete recovery of the displaced phase fluid or a formation of liquid bridge owing to trapping of the displaced phase fluid between two consecutive porous block is possible. In particular, we show existence of two distinctive regimes of dynamics, and in a regime diagram, we portray the influence of the key governing parameters viz. substrate wettability and pore fraction on the operating condition.

(4) We also observe a second mechanism of fluid trapping that can occur even after the interface has completely recovered after confronting one obstacle. This mechanism of fluid trapping essentially occurs when the curvature of the recovered interface at the line of symmetry is very small. In such cases, it is possible that the two ends of the moving interface touch the downstream obstacle after it travels for a while leading to formation of a trapped liquid bridge.

(5) We show that the size and shape of the liquid bridge formed between two consecutive porous blocks does not alter once it attains a steady-state situation. We further demonstrate that no flow can cross the surface of the bridge, primarily attributable to the location of the bridge where it forms at a downstream of two consecutive blocks.

The inferences obtained from the presnt study can be far-reaching, as far as the technological implications are concerned. We believe that the present study may enhance the understanding of imbibiton dynamics from a fundamental perspective of contact-line motion at the pore scale. We also believe that the systematic interrogation of several interesting insights as delineated in the present study will bridge an important gap in the lietrature, and the regime diagram may guide the practicing professionals to engineer and control transport through porous structures, which may bear far-reaching consequences in several areas of application.


[1] P. M. Adler and H. Brenner, Annu. Rev. Fluid Mech. **20**, 35 (1988).
[2] W. L. Olbright, Annu. Rev. Fluid Mech. **28**, 187 (1996).
[3] M. Alava, M. Dub'e, and M. Rost, Adv. Phys. **53**, 83 (2004).
[4] J. J. L. Higdon, J. Fluid Mech. **730**, 1 (2013).
[5] R. Chandler, J. Koplik, K. Lerman, and J. F. Willemsen, J. Fluid Mech. **119**, 249 (1982).
[6] J. C. Parker, R. J. Lenhard, and T. Kuppusamy, Water Resour. Res. **23**, 618 (1987).
[7] M. Blunt, Curr. Opinion Colloid. Interface Sci. **6**, 197 (2001).
[8] K. E. Thompson, AIChE J. **48**, 1369 (2002).
[9] Y. D. Shikhmurzaev and J. E. Sprittles, J. Fluid Mech. **694**, 399 (2012).
[10] M. Schmucki, M. Pradasi, G. A. Pavliotis and S. Kalliadasis, Proc. R. Soc. A **468**, 3705 (2012).
[11] W. Kozicki and C. Tiu, Rheol. Acta. **27**, 31 (1988); R. J. Marhshall and A. B. Metzner, Ind. Eng. Chem. Found. **6**, 393 (1967).
[12] S. R. Pride and E. G. Flekkøy, Phys. Rev. E **60**, 4285 (1999).
[13] M. G. Gerritsen and L. J. Durlofsky, Ann. Rev. Fluid Mech. **37**, 211 (2005).
[14] L. M. Abriola and G. F. Pinder, Water Resour. Res. **21**, 11 (1985).

[15] L. M. Abriola and G. F. Pinder, Water Resour. Res. **21**, 19 (1985).
[16] T. Kuppasamy, J. Sheng, J. C. Parker, and R. J. Lenhard, Water Resour. Res. **23**, 625 (1987).
[17] R. Lenormand and E. Touboul, J. Fluid Mech. **189**, 165 (1988).
[18] B. H. Kueper and E. O. Frind, Water Resour. Res. **27**, 1059 (1991).
[19] B. H. Kueper, W. Abott, and G. Farquhar, J. Contam. Hydrol. **5**, 83 (1989).
[20] A. Rimmer, J.-Y. Parlange, T. S. Steenhuis, C. Darnault, and W. Condit, Transp. Porous Med. **25**, 205 (1996).
[21] H. Darcy, *Les fontaines publiques de la ville de Dijon* (Dalmont, Paris, 1856).
[22] L. A. Richards, Physics **1**, 318 (1931).
[23] F. Kalaydjian, Transp. Porous Med. **2**, 537 (1987).
[24] C. R. Faust, J. H. Guswa, and J. W. Mercer, Water Resour. Res. **25**, 2449 (1989).
[25] P. A. Forsyth, Adv. Water Res. **11**, 74 (1988).
[26] J. J. Kaluarachchi and J. C. Parker, Water Resour. Res. **25**, 43 (1989).
[27] M. Osborne and J. Sykes, Water Resour. Res. **22**, 25 (1986).
[28] C. W. Hirt and B. D. Nichols, J. Comput. Phys. **39**, 201 (1981).
[29] S. Osher and J. A. Sethian, J. Comput. Phys. **79**, 12 (1988).
[30] J. A. Sethian, *Level Set Methods and Fast Marching Methods* (Cambridge University Press, Cambridge, 1999).
[31] M. Sussman and E. G. Puckett, J. Comput. Phys. **162**, 301 (2000); B. Ray, G. Biswas, and A. Sharma, J. Fluid Mech. **655**, 72 (2010).
[32] D. M. Anderson, G. B. McFadden, and A. A. Wheeler, Annu. Rev. Fluid Mech. **30**, 139 (1998).
[33] V. E. Badalassi, H. D. Ceniceros, and S. Banerjee, J. Comput. Phys. **190**, 371 (2003).
[34] D. Jacqmin, J. Fluid Mech. **402**, 57 (2000).
[35] X.-P. Wang, T. Qian, and P. Sheng, J. Fluid Mech. **605**, 59 (2008).
[36] H.-Y. Chen, D. Jasnow, and J. Viñals, Phys. Rev. Lett. **85**, 1686 (2000).
[37] P. A. Thompson and M. O. Robbins, Phys. Rev. Lett. **63**, 766 (1989).
[38] A. J. Briant, A. J. Wagner, and J. M. Yeomans, Phys. Rev. E **69**, 031602 (2004).
[39] P. Seppecher, Int. J. Eng. Sci. **34**, 977 (1996).
[40] L. M. Pismen and Y. Pomeau, Phys. Rev. E **62**, 2480 (2000).
[41] J. W. Cahn and J. E. Hilliard, J. Chem. Phys. **28**, 258 (1958).
[42] J. W. Cahn and J. E. Hilliard, J. Chem. Phys. **31**, 688 (1959).
[43] H. Ding and P. D. M. Spelt, Phys. Rev. E **75**, 046708 (2007).
[44] D. Jacqmin, J. Comput. Phys. **155**, 96 (1999).
[45] Y. Q. Zu and S. He, Phys. Rev. E **87**, 043301 (2013).
[46] T. Qian, X.-P. Wang, and P. Sheng, Phys. Rev. E **68**, 016306 (2003).